Available online at www.sciencedirect.com

ScienceDirect

Acta Materialia 63 (2014) 130–139

Acta MATERIALIA

www.elsevier.com/locate/actamat

Heterogenous void growth revealed by in situ 3-D X-ray microtomography using automatic cavity tracking

L. Lecarme [a], E. Maire [c], A. Kumar K.C. [b], C. De Vleeschouwer [b], L. Jacques [b], A. Simar [a,*], T. Pardoen [a,*]

[a] *Institute of Mechanics, Materials and Civil Engineering, Université catholique de Louvain, B-1348 Louvain-la-Neuve, Belgium*
[b] *Institute of Information and Communication Technologies, Electronics and Applied Mathematics, Université catholique de Louvain, B-1348 Louvain-la-Neuve, Belgium*
[c] *MATEIS UMR5510, INSA-Lyon, F-69621 Villeurbanne, France*

Received 20 July 2013; accepted 9 October 2013
Available online 13 November 2013

Abstract

Ductile fracture by nucleation, growth and coalescence of internal voids is the dominant fracture mechanism in metals at ambient temperature. Micromechanics-based models for each elementary mechanism have been developed and enhanced over the past 40 years, allowing microstructure-informed failure predictions essentially assuming homogeneous damage evolution. In situ 3-D microtomography has been instrumental to assess these models from experimental evolution of average void density and size. Nevertheless, statistical effects on the damage evolution associated with microstructure distribution heterogeneities have not yet been addressed quantitatively due to the difficulty in tracking individual cavities. Here, we show, from 3-D in situ microtomography characterization of a Ti–6Al–4V alloy, factor ~4 variations among the growth rate of individual cavities undergoing the same stress triaxiality and same plastic deformation. This statistical analysis has been made possible owing to an advanced tracking algorithm relying on a graph-based data association approach initially developed for the field of computer vision to track target motions. The measured variations originate from void shape and crystal orientation effects, as well as from local constraints changes due to the presence of two phases with different strengths.

Keywords: Titanium alloys; X-ray tomography; Damage initiation; Growth kinetics; Data association

1. Introduction

Metals usually fail at ambient temperature through the nucleation, growth and coalescence of small internal voids. This sequence of microscale damage mechanisms is at the origin of the moderate to high ductility of metals. The physics of ductile fracture has been a subject of intense investigations in the solid mechanics and material science communities since the late 1960s, with the pioneering micromechanics-based modeling works of McClintock [1] and Rice and Tracey [2]. Advanced models for the three stages of nucleation, growth and coalescence of voids have been proposed and enhanced over the years to become more and more realistic (see the reviews of Benzerga and Leblond [3] and Pardoen et al. [4]). The most recent void nucleation models properly account for the load transfer within elastic or elastoplastic inclusions that initiate the damage process [5,6], involving statistical effects [7]. Extensions of the classical Gurson model [8] for the void growth stage involve void shape effects [9,10], kinematic hardening [11], plastic anisotropy [12–14], viscoplastic effects [15–17], void rotation and shear effects [18,19]. Over the last 10 years, progress has been made in the description of void coalescence, many of the models relying on the Thomason approach [10,20–24]. The construction of these theoretical

* Corresponding authors. Tel.: +32 10473565 (A. Simar), +32 10472417 (T. Pardoen).
E-mail addresses: aude.simar@uclouvain.be (A. Simar), thomas.pardoen@uclouvain.be (T. Pardoen).

1359-6454/$36.00
http://dx.doi.org/10.1016/j.actamat.2013.10.014

models has been guided and validated through comparison with finite-element void cell simulations (e.g. [10,16,17,23,25]), with indirect experiments such as density measurements [26], or with direct observation using 2-D sections (e.g. [27]) and, better, with 3-D tomography methods [28–32]. For simple materials, specialists are close to predicting failure based only on microstructure information, which is essential for a variety of applications of metals in critical structural components. As a result, the current state of the art is well developed and validated with sound theoretical and physical foundations, albeit essentially for sufficiently homogeneous materials. However, major questions remain in the case of heterogeneous materials, which is the rule rather than the exception.

By heterogeneities, we mean that both the distribution of second phases that determines the distribution of the voids and heterogeneities in the local mechanical properties must be considered. The distribution of second phases can be spatially clustered, and their sizes and shape can also vary a lot within the same microstructure. The strength and toughness of the particles can significantly vary as a function of their size but also due to variations in chemical composition. The strength of the matrix depends on crystal orientation for voids located inside grains, or on the orientation of the connecting grains in the case of voids sitting along grain boundaries or at triple junctions. Matrix response can also depend on gradients of microstructure near grain boundaries or near second phases. The result of these heterogeneities can influence the three stages of damage with cavities that can locally coalesce while others have just been nucleated, leading to cascades of coalescence, with variations in the sizes of the cavities and with complicated interaction effects.

There have been several attempts in the literature to address some issues related to heterogeneities. The inhomogeneity could be due to a statistical distribution of the matrix/particle cohesion stress about a mean interfacial stress (see e.g. [33]) or to local microplasticity effects in relation to crystallographic details (see e.g. [34]). The variation in the local nucleation rate was investigated in duplex stainless steels [35,36] using interrupted tests. The analysis has shown that particle clusters lead to nucleation rates that are much larger than the mean nucleation rate. Several authors have shown that heterogeneities in the void distributions, do not significantly affect the void growth rates [37–39]. However, small voids in the neighborhood of large cavities can grow much faster than in a single-sized population [40,41]. Void cell calculations performed with a crystal plasticity model show that the crystal orientation can modify the void growth rate by a factor of two (e.g. [42,43]). Advanced 3-D void cell simulations have allowed the complex configuration of several voids to be addressed to analyze the interaction effects, which mainly affect coalescence [39,44]. More simple cellular automaton-type approaches are also possible to capture cluster effects on coalescence and cracking [45]. Regarding heterogeneties in the local properties, several authors have analyzed the effect of the location of voids at the interface between two phases with different flow properties [46–48], of the presence of soft zones near grain boundaries [49–51] or inside welds on void growth (e.g. [52,53]). Recently, probably the most advanced computational method involving crystal orientation effects and realistic distribution of cavities has been proposed by Lebensohn, showing the local effects of crystal orientations on void coalescence [54].

Experimentally, the most attractive approach to investigate the impact of heterogeneities in the physics of ductile failure is offered by 3-D tomography. Today, resolutions of around 1 μm are commonly attained with aquisition times on the order of 5 min. Resolutions down to 100 nm are also possible, but the acquisition time required is much larger (120 min). However, up to now, analysis of the tomographic data has been mainly focused on mean porosity evolution, as well as qualitative observations from reconstructed 3D images. The limitation to addressing heterogeneous damage behavior with a quantitative approach is the difficulty in tracking cavities individually, except for the largest ones [30].

The goal of this paper is to present a novel 3-D microtomography-based approach in which an advanced tracking algorithm was applied to automatically monitor the evolution of a wide range of individual cavities. The tests were performed on Ti–6Al–4V notched tensile test specimens and were motivated by applications in turboengines, where the question of fracture strain is a key issue. In addition to validating the new data reduction scheme for tomography, this first application of the method shows very significant variations in the void growth rates of individual cavities, even after careful treatment of the local stress and strain values. Different sources of heterogeneities are discussed. This approach opens new avenues to quantitatively address heterogeneous effects in ductile failure.

The outline of the paper is as follows. The microstructure and properties of the material, as well as the X-ray microtomography technique, are first introduced. Subsequently, the finite element procedures and the tracking algorithm are described. The results on the evolution of cavities are then presented and discussed according to three approaches: (i) all of the cavities together, (ii) all of the cavities individually and (iii) a particular population of cavities (the largest ones).

2. Experimental methods

2.1. Material

The material was cut from Ti–6Al–4V ingots obtained by extrusion, involving 50% reduction at 940 °C, followed by annealing at 700 °C. The microstructure consists of primary hexagonal α grains embedded in a matrix composed of alternating lamellae of secondary α and body-centered cubic β (see Fig. 1). Electron backscatter diffraction analysis indicates that the α phase volume fraction is equal to 94%. The stress–strain response of the material in uniaxial

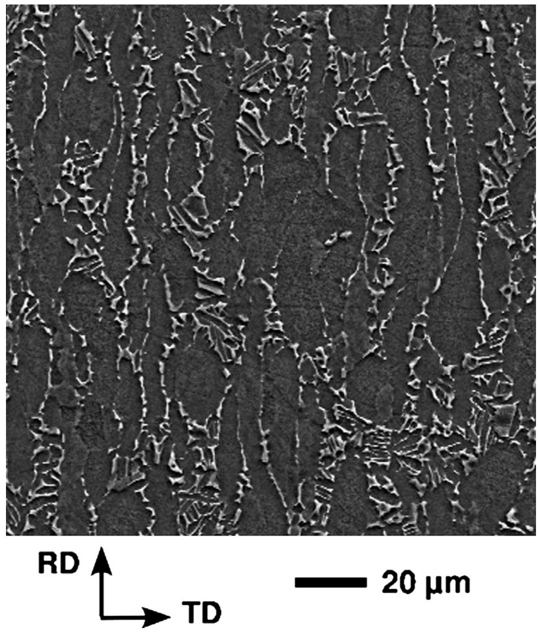

Fig. 1. Scanning electron micrograph of a section of the material. The α phase appears in dark gray and the β phase appears in white.

tension is given in Fig. 2. The yield stress at 0.2% strain is 877 MPa and the true strain at necking is 0.09.

2.2. X-ray microtomography

The tomography measurements were performed at the ID15A beamline at the European Synchrotron Radiation Facility (ESRF) in Grenoble, France. More details on the set-up are given in Ref. [29]. A dedicated in situ tensile testing machine described in Ref. [28] was mounted on the rotation stage of the tomography set-up. The stage rotates at a constant speed while the tensile test is continuously performed at a displacement rate of 2×10^{-4} m s^{-1}. The tensile force F applied on the specimen is recorded at all times. The data aquisition is made at regular discrete time steps, with a voxel size of 1.06 μm^3. The geometry of the test specimen is given in Fig. 3. Only the central region in the minimum section has been imaged.

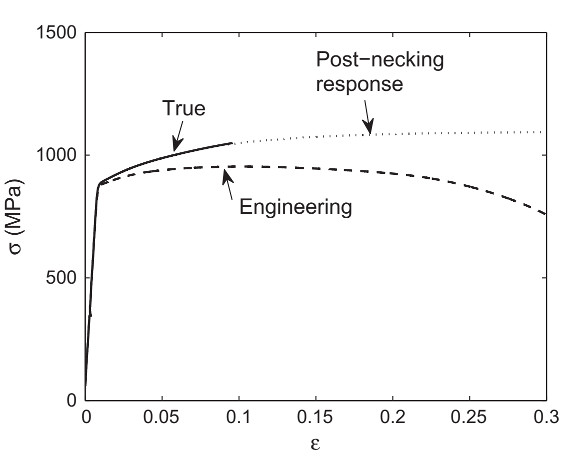

Fig. 2. Macroscopic engineering and true stress–strain curve of the material. The true post-necking response, identified by an inverse numerical procedure, is also provided.

The raw volumes obtained from the reconstruction of the tomography scans were then median filtered and thresholded, according to the method described in [30]. This procedure allows separating the voids from the Ti–6Al–4V matrix.

Only the central zone of the tensile specimen shown in Fig. 3 is selected for damage quantification. It was chosen to be a cubic volume of side 200 μm. This central sub-volume undergoes the largest stress triaxiality and thus the fastest damage rates [26].

3. Data reduction schemes

3.1. Finite elements simulation of the test

The magnitude of the stresses and strains in the center of the specimen were calculated by finite element simulations using the commercial code Abaqus Standard [55]. The mesh was created with the open-source mesh generator Gmsh [56]. It is composed of axisymmetric second-order triangular elements. The material is modeled using isotropic J2 flow theory, with the hardening law extracted from the uniaxial true stress–true strain curve of Fig. 2 and extended to large strain through an iterative procedure [57].

In order to simplify the computation, the cubic sub-volume of interest is modeled as a cylinder of diameter and height equal to 200 μm. Due to the axisymmetry of the problem, only a section of the test specimen is modeled. The average values of the stresses and strains in the test volume are calculated by averaging over all the elements of the small central cylinder. The average equivalent plastic strain and the average stress triaxiality are given by

$$\varepsilon_{sub} = \frac{1}{V_{cyl}} \sum_{i=1}^{n} \left(\varepsilon_{eq}^{p}\right)^{i} V^{i}, \tag{1}$$

$$T_{sub} = \frac{1}{V_{cyl}} \sum_{i=1}^{n} \frac{\sigma_h^i}{\sigma_{eq}^i} V^{i}, \tag{2}$$

with V_{cyl} the volume of the cylinder and n the total number of elements in the cylinder; V^i, $\left(\varepsilon_{eq}^{p}\right)^{i}$, σ_h^i and σ_{eq}^i are respectively the volume, the equivalent plastic strain, the hydrostatic stress and the equivalent stress in every element of the cylinder.

The local values of the stress triaxiality and of the equivalent plastic strain were also recorded at different reference locations in the volume analyzed by tomography (see Fig. 4). The local stress triaxiality T_{loc} and equivalent plastic strain ε_{loc} corresponding to the location of a cavity are calculated by linear interpolation of the values from the nine reference positions, depending on their coordinates.

3.2. Tracking algorithm

Once the cavities have been detected and their geometrical features have been calculated independently at different

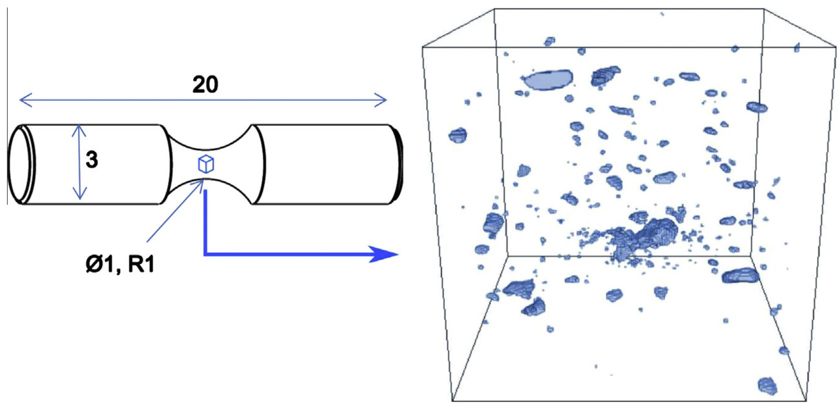

Fig. 3. 3-D visualization of the sub-volume used to characterize damage (dimensions in mm) and schematic location in the tested specimen.

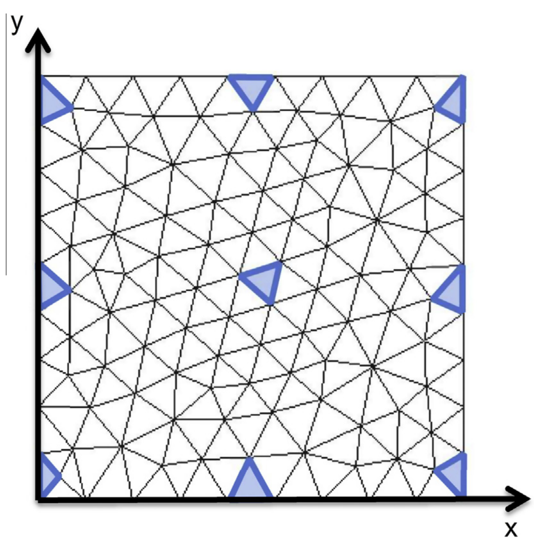

Fig. 4. Reference elements from which the local stress triaxiality and equivalent plastic strain have been extracted.

time instants, they have to be associated across time so as to measure how they evolve. This problem is commonly referred to as data association, and has been extensively studied in other domains. In the field of computer vision, such approaches have been used to track the movement of people, vehicles, biological cells, etc.

Graph-based approaches have been widely adopted to solve the data association problem. In this framework, each detection defines a node in the graph, and the cost of an edge between two nodes is defined to decrease with the likelihood that the two nodes correspond to the observations of the same physical cavity at distinct time instants. Shortest paths [58] are then computed to find the most probable associations of the cavities along the timeline. Turning the general framework into an actual solver most often requires accounting for the specificities of the problem at hand. This is because not only the physical constraints, governing the dynamics of the targets (people, cells, cavities, etc.), but also the observation models are particular to each problem. Cavity tracking has several specificities, namely: (i) the detection process has no false or missed detections; (ii) the cavity volume increases with time; and (iii) two cavities can locally coalesce into a bigger one in an instant. These specificities make the tracking of cavities different from tracking other targets, like people or vehicles.

In this section, we formalize the problem of tracking cavities as finding shortest path(s) in a graph, first by providing a formal definition of the graph that is used to track cavities and then by describing how the graph is exploited to associate cavities across time based on shortest path computations.

3.2.1. Graph definition for cavity tracking

As an input, the algorithm receives the set of candidate cavities detected independently at each time instant. Each detection d is characterized by the vector

$$d = (t, c, v),$$

where $t \in \mathbb{Z}^+$ is the time instant, and $c \in \mathbb{R}^3$ and $v \in \mathbb{R}$ are the centroid and the volume of a cavity, respectively. We define a graph $\mathcal{G} = (\mathcal{V}, \mathcal{E}, \mathcal{C})$ by

– a set of nodes $\mathcal{V}$, in which the node u_i corresponds to the cavity detection d_i. We denote the nodes occurring at time t by V_t.
– a set of edges, $\mathcal{E} \subseteq \mathcal{V} \times \mathcal{V}$, defining the connectivity between the nodes in $\mathcal{V}$. As there are no missed detections, there is no need to bridge potential detection(s) gaps, and the edges have only to be created between the nodes that are consecutive in time.
– a set of costs, $\mathcal{C} : \mathcal{E} \rightarrow \mathbb{R}^+$, defining the costs of the edges in $\mathcal{E}$, as detailed below.
– two virtual nodes, called the *source* and the *sink* nodes. They are connected to all other nodes by creating so-called virtual edges, so as to allow for a sequence of cavities to initiate or terminate at any instant in time, despite the shortest paths always being computed between the source and the sink.

A sample graph, with virtual nodes and edges, is shown in Fig. 5(a).

To complete the graph definition, we now define the (virtual) edges costs. As described above, we denote the ith node as $u_i \in \mathcal{V}$. It corresponds to detection d_i, and its features are $\{t_i, c_i, v_i\}$. The cost of associating two nodes u_i and u_j, denoted by $C(u_i, u_j)$, depends on the centroid and the volume of the detected cavities, and is defined by:

$$\mathcal{C}(u_i, u_j) = \begin{cases} \|c_i - c_j\| & \text{if } t_j = t_i + 1, (v_i \leqslant v_j) \text{ or } (|v_i - v_j| \leqslant \tau_{\text{vol}}), \\ \infty & \text{otherwise}, \end{cases} \tag{3}$$

where $\|\cdot\|$ measures the Euclidean distance between c_i and c_j, and τ_{vol} is the tolerance applied to the estimation of cavity volume difference and accounts for possible measurement errors. Empirically, we set $\tau_{\text{vol}} = 3$ voxels. Note that, when relevant, the cost function in Eq. (3) can be adapted to compensate for the expected displacement of the cavity between consecutive observations. For instance, the displacement of a cavity between consecutive observations corresponding to different deformations is expected to be non-zero, and increases with the distance to a fixed material point. The cost $\|c_i - c_j\|$ should then be replaced by the L_2-norm of the difference between the observed and expected displacements.

In contrast to regular edges, the cost of a virtual edge is defined such that the edges between the nodes in consecutive frames are favoured over the virtual edge, which implicitly promotes long tracks. Specifically, the cost is defined as being proportional to the time difference between a node and the sink node (u_{sink}) and source node (u_{source}) as

$$\begin{aligned} \mathcal{C}(u_{\text{source}}, u_i) &= \beta_1 \cdot (t_i - t_{\text{start}}), \\ \mathcal{C}(u_i, u_{\text{sink}}) &= \beta_2 \cdot (t_{\text{end}} - t_i), \end{aligned} \tag{4}$$

where t_{start} and t_{end} are the start and end time instances; and β_1 and β_2 must be calibrated. Since $\beta_2 \gg \beta_1$ promotes long tracks, we set $\beta_1 = 5$ and $\beta_2 = 100$ by experimental validations.

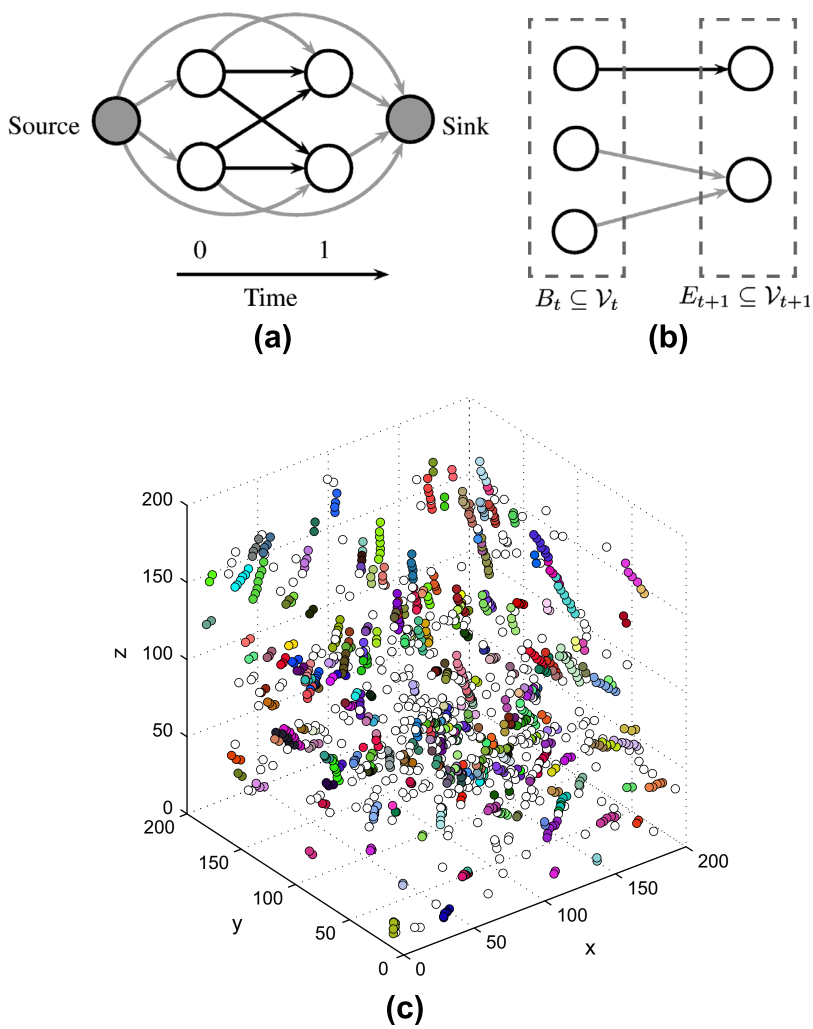

Fig. 5. Data association scheme and results. (a) Sample graph consisting of two time instants and two detections at each instant. The Source node, sink node and virtual edges are represented in gray. (b) Different cases in progressive matching. One-to-one matching is shown with black arrows. In this case, the connection is considered to be reliable. Many-to-one matching is shown in gray. This might happen if two cavities coalesce. Other possible cases are not considered during the progressive matching. (c) Cavity tracking in the cubic volume. The circles indicate the center of mass of the cavities. Each color represents a different track. The cavities not belonging to any track (or belonging to a track composed of a single step) appear in white. (For interpretation of the references to color in this figure legend, the reader is referred to the web version of this article.)

3.2.2. Computation of shortest paths for cavities association

Once the graph has been defined, we compute the shortest paths between the source and sink nodes to aggregate the cavity detections into tracks, each track describing the temporal evolution of a single cavity. For this purpose, two solutions are generally considered in the literature. On the one hand, the K-shortest paths solution [59] considers the joint computation of those K-shortest tracks. On the other hand, the embedding of the Dijkstra's shortest path algorithm [58] into a greedy process iteratively computes a shortest path and removes it from the graph until no more tracks can be found in the graph. Since the joint estimation of shortest paths is computationally expensive,[1] the greedy approach has been selected to solve our cavity tracking problem.

The cavity coalescence process needs to be addressed to extend the conventional greedy approach to the cavities association problem. The possible coalescence of cavities is accounted for by investigating the associations of cavities detected at two consecutive time instants before launching the greedy shortest path computation process. The aggregation of cavities resulting from this initial investigation also limits the growth of the number of nodes in the graph with time, which in turns reduces the global computational load. The aggregation of cavities detected at consecutive time instants is described as follows.

Primarily, the local aggregation process only retains/considers the edges (between detections at two consecutive time instants) whose cost is lower than some predefined threshold, $\tau_{\max}$. In our experiments, $\tau_{\max} = 10$ is chosen.[2] Let $B_t \subseteq V_t$ and $E_{t+1} \subseteq V_{t+1}$ be the sets of vertices for which the cost is lower than $\tau_{\max}$. Then, as shown in Fig. 5(b), we distinguish the following two association topologies during the initial phase:

– **One-to-one**: a vertex $u_i \in B_t$ is connected to a single vertex $u_j \in E_{t+1}$, and no other connection links V_t to u_j. It is shown with a black arrow in Fig. 5(b). In this case, we consider that the association is reliable and combine u_i and u_j into a single supernode that is connected to V_{t-1} and V_{t+2} in the same way as u_i and u_j, respectively.

– **Many-to-one**: several vertices in B_t are connected to a single node $u_j \in E_{t+1}$. This case is depicted with gray arrows in Fig. 5. Since cavities can merge into bigger cavities, we consider this to be a potential coalescence and perform hypothesis testing. We hypothesize that, if the cavities coalesce, then the resulting volume of the cavity should not be smaller than the sum of all coalescing cavities, and the centroid of the resulting cavity should be close to the mean of the centroids of the merging cavities. If all conditions are satisfied, we accept the coalescence hypothesis.

Other association possibilities are ignored during progressive matching. Fig. 5(c) presents the outcome of the tracking algorithm.

[1] The joint estimation of k shortest paths requires $O(k(m + n\log n))$, where m is the number of edges and n is the number of nodes, whereas the greedy approach requires less than $O(k(m + n))$. It is noteworthy that m and n decrease at each iteration of the greedy approach.

[2] The value of $\tau_{\max}$ is typically derived from the edges costs distribution, in a conservative way, so that only reliable connections are considered.

4. Results

4.1. Macroscopic behavior

The minimum cross-section area S of the specimen was measured on the macroscopic images taken during the test in order to calculate the average true macroscopic axial strain ε_{mac} in this section at each step, using

$$\varepsilon_{mac} = \ln\left(\frac{S_0}{S}\right), \tag{5}$$

where S_0 is the initial cross-section area. Note that this expression excludes any effect of porosity on the volume change during straining. Three deformations are thus used: an average equivalent strain over the minimum cross-section ε_{mac}, an average equivalent strain in the volume of analysis ε_{sub} and the local equivalent strain inside the volume ε_{loc}.

The stress triaxiality T_{sub} in the volume used for damage analysis varies from 0.8 to 1.0 during straining of the specimen.

4.2. Average void growth rate based on the average strain

The cavities in the volume of interest were tracked from one deformation step to the next one. Fig. 6(a) shows the evolution of the equivalent radius R of every cavity normalized by its equivalent radius at nucleation R_0 as a function of the average strain ε_{sub}. The equivalent radius of a cavity corresponds to the radius of a sphere having the same volume as the measured cavity. The curves in Fig. 6(a) have been shifted with respect to the strain at nucleation ε_{nuc}, so that the radius evolution of every cavity can be compared. Only the cavities involving a minimum of three detections (i.e. cavities tracked for minimum three consecutive deformation steps) are represented. Significant differences in the growth kinetics are observed, with a factor of four between the slowest and fastest growing voids. The thick (red) line shows the prediction given by the model developed further in Section 4.4.

4.3. Void growth of single cavities

Knowing the values of the stress triaxiality and the strain near a cavity, the Rice and Tracey model [2], corrected by Huang [60], is used in order to rationalize the results presented in Fig. 6(a),

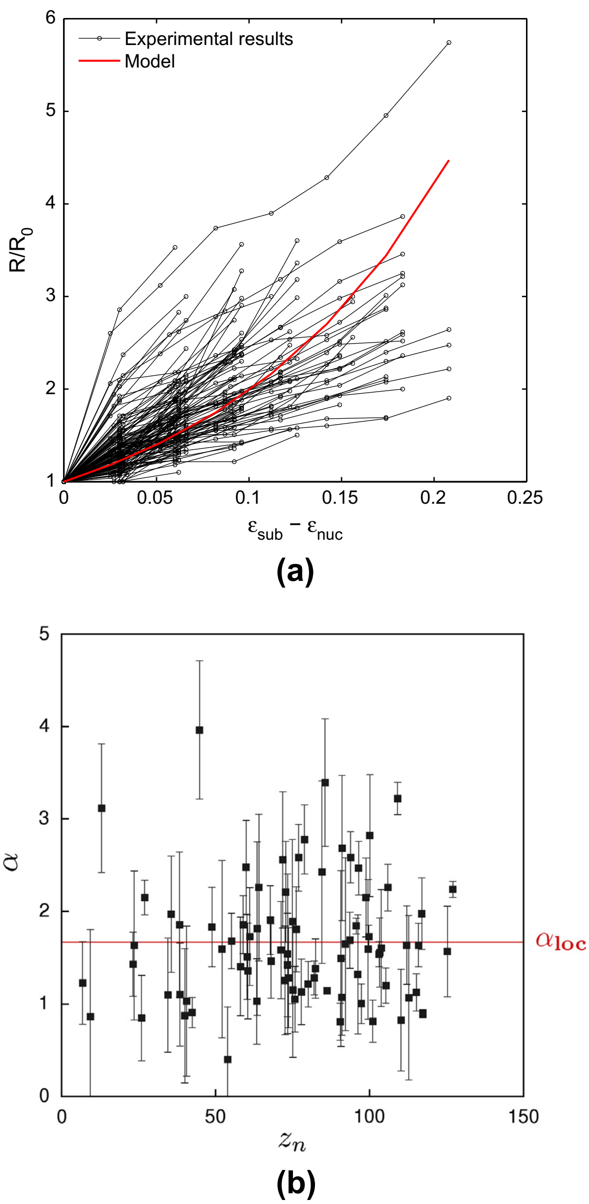

Fig. 6. (a) Evolution of the normalized equivalent radius of every cavity R/R_0, as a function of the average equivalent strain after nucleation $\varepsilon_{sub} - \varepsilon_{nuc}$ within the sub-volume. The gray line shows the prediction from the model. (b) Evolution of α with the distance between the cavity location (at nucleation) and the tensile axis.

$$\frac{dR}{R} = \alpha T_{loc}^{1/4} \exp\left(\frac{3}{2} T_{loc}\right) d\varepsilon_{loc}, \quad (6)$$

where R is the radius of the cavity and α is a constant, theoretically equal to 0.43 [60]. Eq. (6) is valid for $T_{loc} \leq 1$. The idea is that the variations in the void growth rates observed in Fig. 6(a) could originate from the different local triaxiality and plastic strain evolution. The strain difference between each tomography measurement is small enough to consider $d\varepsilon_{loc} \approx \Delta\varepsilon_{loc}$. For a deformation step s, the radius R can be expressed as

$$R^s = R^{s-1} + \Delta R^s, \quad (7)$$

with

$$\Delta R^s = \alpha^s R^{s-1} \left(T_{loc}^s\right)^{1/4} \exp\left(\frac{3}{2} T_{loc}^s\right) \left(\varepsilon_{loc}^s - \varepsilon_{loc}^{s-1}\right). \quad (8)$$

The constant α^s can then be expressed as

$$\alpha^s = \left(\frac{R^s}{R^{s-1}} - 1\right) \left[\left(T_{loc}^s\right)^{1/4} \exp\left(\frac{3}{2} T_{loc}^s\right) \left(\varepsilon_{loc}^s - \varepsilon_{loc}^{s-1}\right)\right]^{-1}, \quad (9)$$

for every deformation step. For each cavity, the average value of α^s during straining is calculated, and simply designated α. Fig. 6(b) shows the evolution of α as a function of its distance with respect to the specimens central axis. A constant value of α would mean that all cavities would follow exactly the same growth kinetics.

The values of α cover a range between 0.6 and 4, with an average value $\alpha_{loc} = 1.67$ and a standard deviation of 0.67. More than 90% are between 0.7 and 2.8, thus involving a factor 4 variation between the void growth rates. The raw data of Fig. 6(a) can also be analyzed more quantitively. If the 10% extreme growth rates are discarded from Fig. 6(a), the variation amounts to a factor 8. This shows that a part of the scatter in Fig. 6(a) was indeed the result of the variations of the stress triaxiality T_{loc} and of the equivalent plastic strain ε_{loc} in the volume of measurement. Furthermore, no particular trend in the evolution of α with the position along the diameter can be identified in Fig. 6(b), showing that the effect of T_{loc} and ε_{loc} on the kinetics of void growth for a single cavity is correctly rationalized by the Rice and Tracey model.

4.4. Growth of a population of cavities

Another possible way to quantitatively analyze the damage evolution is to study a group of cavities and anticipate the effects of size or interactions on the growth kinetics. The largest cavities are interesting, since they are the most influential on the overall damage of the material [29]. Landron et al. [30] demonstrated that the evolution of the 20 largest cavities is close to the that of single large cavities. The largest cavities are considered to always be the same from one deformation step to another. The tracking algorithm is therefore not necessary for this analysis. Using the same method as for single cavities, the Rice and Tracey model corrected by Huang can be applied to the 20 largest cavities in the sub-volume of interest

$$\frac{dR}{R} = \alpha_{20} T_{sub}^{1/4} \exp\left(\frac{3}{2} T_{sub}\right) d\varepsilon_{sub}, \quad (10)$$

with T_{sub} and ε_{sub} the average values of the stress triaxiality and the equivalent plastic strain in the sub-volume. Using Eqs. (7)–(9) for the 20 largest cavities, the average α_{20} during straining is $\alpha_{20} = 1.89$, close to the mean $\alpha_{loc} = 1.67$ given above. This shows that the difference in void growth rate among the cavities is not caused by a difference in void size. This is confirmed by the plot of Fig. 8 which associates with each cavity initial radius R_0 the corresponding α.

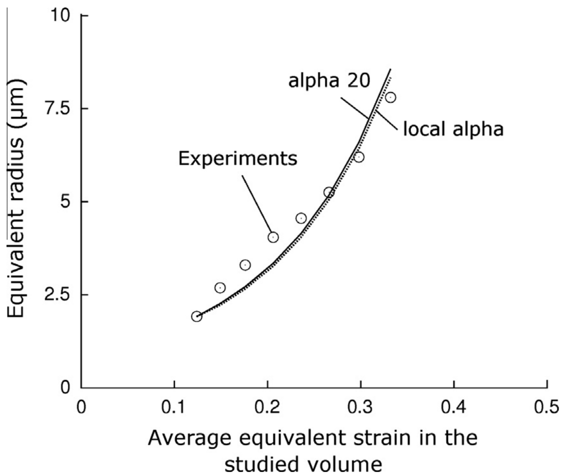

Fig. 7. Evolution of the average equivalent radius R with the average strain in the sub-volume ε_{sub} measured experimentally and predicted by the Rice and Tracey model using two different α parameters.

5. Discussion

The discussion will address three important points. First, several origins for the variations in the void growth rates will be proposed. Then explanations will be provided for the high value of the average α factor of 1.67 when compared to the 0.43 theoretically predicted by Huang [60]. The rate of growth of a void depends on many factors (see the introduction).

(i) Even though the "experimental" factor α has been calculated based on the local stress triaxiality and effective plastic strain, these quantities can still vary very locally as a function of the position of the void with respect to the two phases present in Ti–6Al–4V. As explained by Li [46] and recently addressed in more details by Yerra [48], voids always tend to grow much faster in the softer phase due to an increased local stress triaxiality, which depends directly on the strength mismatch between the two phases. The increased stress triaxiality is due to the constraint effect induced by the hard zone on the softer zone, as observed in other systems (see the introduction). The level of confinement depends on the thickness and shape of the soft zone regions compared to the harder zones. We will come back to this point in the second part of the discussion. The idea here is that the confinement can change significantly from one location to another in the microstructure, and can lead to significant differences in the void growth rate.

(ii) The crystallographic orientation of the grain(s) surrounding the voids can have several effects. First, it directly influences the void growth rate. As mentioned in the introduction, several authors have shown that the void growth rate can change by a factor of up to two when considering the most and least favorable crystal orientations [42,43]. The effects are more marked for hexagonal close-packed crystals. Furthermore, coming back to point (i), the local crystal orientation can also dictate local variations of the stress triaxiality and of the strain level in the microstructure.

(iii) Interaction effects are usually considered to be quite weak between voids of the same size, but, as indicated in the introduction, small voids in the close neighborhood of large voids can grow much faster [40,41]. Usually larger voids come from larger inclusions, which lead to early nucleation [61], while smaller voids nucleate later, with their growth possibly influenced by the proximity of larger voids. Nevertheless, as explained in the previous section and further analyzed by looking at the evolution of α vs. the size of the void (Fig. 8), no such effect has been identified here.

(iv) As explained in Ref. [10], flat voids grow faster than rounded or elongated ones. Depending on the void nucleation conditions, the initial voids can be quite flat in the Ti–6Al–4V alloys when resulting from a decohesion between α and β phase, or more rounded.

The α_{loc} parameter obtained for the present material is approximately 1.67, while the one calculated theoretically by Huang is 0.43 [60]. The difference between these two values could have many origins. The Rice and Tracey analysis refined by Huang describes the growth of a single void in an infinite perfectly plastic matrix, while the real material presents a non-dilute fraction of voids, growing in a strain hardening matrix. Both cavity interaction [62] and strain hardening [10,23] tend to accelerate void growth, hence leading to a higher value of α_{loc}. Furthermore, Li and Guo [46] showed that a void present at a bimaterial interface with a yield strength ratio of 2 grows more than twice as quickly as a void in a single material, whatever its yield

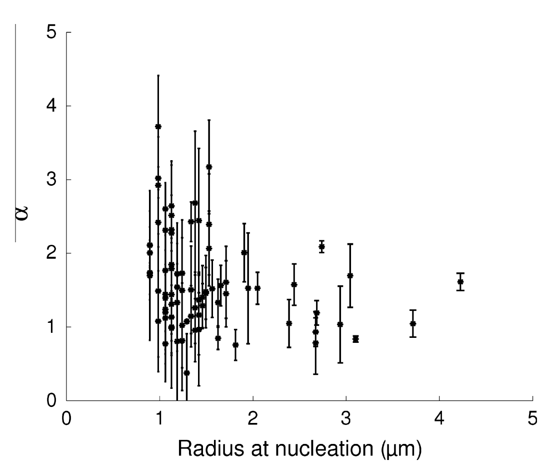

Fig. 8. Parameter α of the Rice and Tracey model as a function of the radius of the cavity at nucleation.

strength. Yerra et al. [48] also showed the influence of the strain hardening parameters mismatch on void growth rate.

The analysis of the tomographic data supplemented by the cavity tracking algorithm also verifies the validity of studying only the 20 largest cavities of the population to determine the α parameter of the Rice and Tracey model. Indeed, the results are sensibly the same whether one computes it from the average evolution of the 20 largest cavities or whether one considers the mean value α_{loc} of all the α parameters obtained from every cavity evolution (see Fig. 7). This validates the approach used in Refs. [29–31] proposing that the study of the 20 largest cavities gives an accurate measurement of the growth of single voids. This type of study is therefore particularly appropriate when the cavity tracking technique is not available. Note that size effects on void growth are expected when the diameter of the voids is below 1 μm [63].

6. Conclusions

An advanced tracking algorithm has been developed for the analysis of in situ 3-D microtomographic data of deformed metallic specimens in order to follow the evolution of cavities which nucleate, grow and coalesce. The algorithm has been applied to data collected on the Ti6Al4V alloy under tension. The main outcomes are as follows:

(i) The tracking algorithm is capable of following the evolution of cavities individually, accounting for the coalescence process during which two cavities group together. There is still room to improve the algorithm and to make it more efficient, by introducing more physical insight, e.g. using a predicted strain field to give a better estimate of the movement of a cavity between two successive microtomography images.
(ii) After careful data reduction analysis, a factor 4 difference among the growth rates of individual cavities undergoing the same stress triaxiality and plastic deformation is obtained, leading to significant heterogeneity in the ductile failure process. This heterogeneity adds to the fact that cavities do not nucleate at the same deformation and not with the same initial size.
(iii) The origin of the distribution in the void growth rates has been related to the effect of the local crystal orientation and to the impact of the two-phase structure involving local variations of the constraint on plastic flow, and thus to local changes in stress triaxiality not accounted for by our homogenous J2 plasticity finite element model.

The implications of this study are numerous. First, the new tracking strategy (with a lot of further possible enhancements) can be applied to both old and new data to greatly enrich the amount of information that can be extracted, with a statistical value. Second, the material science and solid mechanics communities interested in damage and failure will be pushed to further investigate sources of heterogeneities in the fracture process in not only metallic but also ductile polymeric materials. Is this large dispersion in the void growth rates typical only of the titanium alloy studied here (which is an important structural material) or does it apply more general to a vast number of materials? How can we account for these heterogeneities in future ductile failure models? Do these heterogeneities significantly affect the overall resistance to failure? If so, to what extent is it necessary to take them into account to build up reliable failsafe models for critical engineering structures made of ductile metallic alloys?

Acknowledgements

The authors would like to thank the ESRF for the provision of synchrotron radiation at the ID15A beamline and Mario Scheel for his help as local contact. The company Techspace Aero is gratefully acknowledged for providing the material of this study. Computational resources have been provided by the supercomputing facilities of the Université catholique de Louvain (CISM/UCL) funded by the Fonds de la Recherche Scientifique de Belgique (FRS-FNRS). L.L. acknowledges the financial support of the Walloon Region through the Winnomat 2 Fabulous project. A.K.K.C., C.D.V. and L.J. acknowledge the financial support of the FNRS. The authors from the institute of Mechanics, Materials and Civil Engineering acknowledge the financial support from the Interuniversity Attraction Poles Program from the Belgian State through the Belgian Policy agency, contract IAP7/21 "INTEMATE".

References

[1] McClintock FA. J Appl Mech 1968;35:363.
[2] Rice JR, Tracey DM. J Mech Phys Solids 1969;17:201.
[3] Benzerga AA, Leblond JB. Adv Appl Mech 2010;44:169.
[4] Pardoen T, Scheyvaerts F, Simar A, Tekoğlu C, Onck PR. CR Phys 2010;11:326.
[5] Beremin F. Metall Mater Trans A 1981;12:723.
[6] Tekoğlu C, Pardoen T. Int J Plast 2010;26:549.
[7] Chu CC, Needleman A. J Eng Mater Technol 1980;102:249.
[8] Gurson AL. J Eng Mater Technol 1977;99:2.
[9] Gologanu M, Leblond JB, Perrin G, Devaux J. Recent extensions to the Gurson's model for porous ductile metals. In: Suquet P, editor. Continuum micromechanics. New York: Springer-Verlag; 1997.
[10] Pardoen T, Hutchinson JW. J Mech Phys Solids 2000;48:2467.
[11] Besson J, Guillemer-Neel C. Mech Mater 2003;35:1.
[12] Liao KC, Pan J, Tang SC. Mech Mater 1997;26:213.
[13] Benzerga AA, Besson J. Eur J Mech A Solids 2001;20:397.
[14] Keralavarma SM, Benzerga AA. CR Mec 2008;336:685.
[15] Leblond JB, Perrin G, Suquet P. Int J Plast 1994;10:213.
[16] Klöcker H, Tvergaard V. Int J Mech Sci 2003;45:1283.
[17] Lassance D, Fabrègue D, Delannay F, Pardoen T. Prog Mater Sci 2007;52:62.

[18] Scheyvaerts F, Onck PR, Tekoglu C, Pardoen T. J Mech Phys Solids 2011;59:373.
[19] Nahshon K, Hutchinson JW. Eur J Mech A Solids 2008;27:1.
[20] Thomason PF. Ductile fracture of metals. New York: Pergamon Press; 1990.
[21] Zhang ZL, Niemi E. Int J Fract 1995;70:321.
[22] Benzerga AA. J Mech Phys Solids 2002;50:1331.
[23] Lecarme L, Tekoğlu C, Pardoen T. Int J Plast 2011;27:1203.
[24] Tekoglu C, Leblond JB, Pardoen T. J Mech Phys Solids 2012;60:1363.
[25] Koplik J, Needleman A. Int J Solids Struct 1988;24:835.
[26] Pardoen T, Delannay F. Metall Mater Trans A 1998;29:1895.
[27] Chae D, Koss DA. Mater Sci Eng A 2004;366:299.
[28] Buffière JY, Maire E, Cloetens P, Lormand G, Fougères R. Acta Mater 1999;47:1613.
[29] Maire E, Bouaziz O, Di Michiel M, Verdu C. Acta Mater 2008;56:4954.
[30] Landron C, Maire E, Bouaziz O, Adrien J, Lecarme L, Bareggi A. Acta Mater 2011;59:7564.
[31] Thuillier S, Maire E, Brunet M. Mater Sci Eng A 2012;558:217.
[32] Taylor KL, Sherry AH. Acta Mater 2012;60:1300.
[33] Kwon D, Asaro RJ. Metall Trans A 1990;21:117.
[34] Bugat S, Besson J, Pineau A. Comput Mater Sci 1999;16:158.
[35] Pineau A, Joly P. In: Blauel JG, Schwalbe KH, editors. Defect assessment in components – fundamentals and applications. London: ESIS/EGF9; 1991.
[36] Devillers-Guerville L, Besson J, Pineau A. Nucl Eng Des 1997;168:211.
[37] Needleman A, Kushner AS. Eur J Mech A: Solids 1990;9:193.
[38] Huang Y. Mech Mater 1993;16:265.
[39] Thomson CIA, Worswick MJ, Pilkey AK, Lloyd DJ. J Mech Phys Solids 2003;51:127.
[40] Tvergaard V. Int J Solids Struct 1998;35:3989.
[41] Fabrègue D, Pardoen T. J Mech Phys Solids 2008;56:719.
[42] Potirniche GP, Hearndon JL, Horstemeyer MF, Ling XW. Int J Plast 2006;22:921.
[43] Yerra SK, Tekoglu C, Scheyvaerts F, Delannay L, Van Houtte P, Pardoen T. Int J Solids Struct 2010:47;1016.
[44] Segurado J, Llorca J. Acta Mater 2005;53:4931.
[45] Worswick MJ, Chen ZT, Pilkey AK, Lloyd D, Court S. Acta Mater 2001;49:2791.
[46] Li Z, Guo W. Int J Plast 2002;18:249.
[47] Lassance D, Scheyvaerts F, Pardoen T. Eng Fract Mech 2006;73:1009.
[48] Yerra SK, Martin G, Véron M, Bréchet Y, Mithieux JD, Delannay L, et al. Eng Fract Mech 2013;102:77.
[49] Becker R, Needleman A, Suresh S, Tvergaard V, Vasudevan AK. Acta Metall 1989;37:99.
[50] Pardoen T, Dumont D, Deschamps A, Bréchet Y. J Mech Phys Solids 2003;51:637.
[51] Pardoen T, Bréchet Y. Philos Mag 2004;84:269.
[52] Nielsen KL, Pardoen T, Tvergaard V, de Meester B, Simar A. Int J Solids Struct 2010;47:2359.
[53] Simar A, Bréchet Y, de Meester B, Denquin A, Gallais C, Pardoen T. Prog Mater Sci 2012;57:95.
[54] Lebensohn RA, Cazacu O. Int J Solids Struct 2012;49:3838.
[55] ABAQUS. User's Manual. Version 6.3. Providence, RI; 2002.
[56] Geuzaine C, Remacle JF. Int J Numer Method Eng 2009;79:1309.
[57] Simar A, Nielsen KL, de Meester B, Tvergaard V, Pardoen T. Eng Fract Mech 2010;77:2491.
[58] Dijkstra EW. Numer Math 1959;1:269.
[59] Berclaz J, Fleuret F, Turetken E, Fua P. IEEE Trans 2011;33:1806.
[60] Huang Y. J Appl Mech 1991;58:1084.
[61] Huber G, Bréchet Y, Pardoen T. Acta Mater 2005;53:2739.
[62] Marini B, Mudry F, Pineau A. Eng Fract Mech 1985;22:375.
[63] Fleck NA, Hutchinson JW. Adv Appl Mech 1997;33:295.